Journal of
Materials Chemistry A

Materials for energy and sustainability

Accepted Manuscript

This article can be cited before page numbers have been issued, to do this please use: H. Qin, S. LaCroix, M. Kothakonda, M. Yang and Q. Zhao, *J. Mater. Chem. A*, 2026, DOI: 10.1039/D6TA03536A.

ROYAL SOCIETY OF CHEMISTRY

rsc.li/materials-a

View Article Online
DOI: 10.1039/D6TA03536A

Ru-Doped Single-Atom Alloys for Ammonia Decomposition via First-Principles Simulations

Huang Qin,[1#] Sarah LaCroix,[1#] Manish Kothakonda,[1] Ming Yang,[2] and Qing Zhao[1*]

[1] Department of Chemical Engineering, Northeastern University, Boston, MA 02115, United States
[2]Department of Chemical and Biomolecular Engineering, Clemson University, Clemson, SC 29634, United States

***Corresponding Author:** Qing Zhao (E-mail: q.zhao@northeastern.edu)

[#] These authors contributed equally.

Abstract

Ammonia decomposition is an attractive route for on-demand hydrogen production from carbon-free chemicals. However, the rational design of efficient catalysts remains challenging due to intrinsic trade-offs in surface reactivity: catalysts that effectively activate N-H bonds often bind reaction intermediates too strongly, leading to surface poisoning and sluggish product desorption. Ruthenium (Ru) is among the most active metals for this reaction, yet its strong nitrogen adsorption and scarcity limit its practical utilization. Here, we employed first-principles calculations to design single-atom alloys (SAAs), in which isolated Ru atoms are dispersed within 3*d*-5*d* transition-metal hosts to maximize the atom efficiency of Ru while potentially improving catalytic reactivity. We first evaluated the thermodynamic stability of various Ru-doped SAAs against dopant aggregation and subsurface segregation. We then systematically investigated the reaction energetics of ammonia decomposition, focusing on the trade-off between ammonia dehydrogenation and the associative desorption of N_2 and H_2. Thermodynamic screening identified Ru/Fe, Ru/Co, and Ru/Ni SAAs as promising candidates with favorable energetics for associative desorption. Notably, further kinetic analysis revealed that Ru/Fe SAA is highly active for ammonia decomposition, exhibiting reduced barriers for both dehydrogenation and associative desorption compared with pure Ru. In addition, we identified the adsorption energy of atomic nitrogen as an effective thermodynamic descriptor correlating well with catalytic reactivity across the SAAs. This work provides fundamental insights into overcoming catalytic limitations through atomic doping strategies, while demonstrating how SAAs maximize the atomic efficiency of scarce noble metals and guiding the design of more efficient catalysts for ammonia decomposition.

View Article Online
DOI: 10.1039/D6TA03536A

I. Introduction

The transition toward sustainable energy has stimulated growing interest in carbon-free energy resources.[1-3] Hydrogen (H_2) is widely regarded as a promising clean fuel, yet its large-scale utilization is hindered by its low volumetric energy density as a gas and the difficulties in storage and transportation as a liquid.[4, 5] Ammonia (NH_3) has therefore emerged as an attractive hydrogen carrier, combining a high gravimetric capacity of 17.7 wt%,[6] facile liquefaction,[7] and a well-established global infrastructure.[8] Nevertheless, the practical deployment of ammonia as a hydrogen carrier depends critically on the efficient release of H_2 through ammonia decomposition ($2NH_3 \rightarrow N_2 + 3H_2$).[9, 10] Given its significant kinetic barriers, development of active catalysts for this reaction is essential for on-demand hydrogen production.

Despite its promise, developing effective catalysts for ammonia decomposition is challenging because optimal performance necessitates both efficient ammonia activation and facile removal of adsorbed intermediates.[11] Conventional monometallic surfaces usually exhibit a reactivity trade-off between NH_x dehydrogenation and N_2 or H_2 associative desorption steps, such that surfaces that facilitate N-H bond cleavage tend to bind nitrogen-containing species too strongly, whereas those with weaker nitrogen affinity are less effective for ammonia activation. Among known monometallic materials, ruthenium (Ru) remains one of the most active catalytic metals for ammonia decomposition.[12, 13] However, its performance is limited by the difficulty of removing surface nitrogen species, because strongly bound adsorbed nitrogen (*N) can accumulate on the surface, block active sites, and deactivate the catalyst.[14] In contrast, alternative metals with weaker nitrogen binding strength generally lack sufficient activity for ammonia dehydrogenation. More importantly, Ru is a scarce noble metal, limiting its practical applications on a large scale. Therefore, advancing on-demand hydrogen production via ammonia decomposition requires the discovery of catalysts that are active for both N-H bond activation and the removal of *N and *H species, while minimizing reliance on scarce noble metals.

To address these limitations, substantial efforts have been devoted to catalyst design for ammonia decomposition. Experimentally, alloying has emerged as an effective route to simultaneously improve reactivity for ammonia activation and adsorbate removal. Recent studies have shown that Fe-Co bimetallic catalysts supported on MgO can weaken the *N binding strength and significantly improve ammonia decomposition activity,[15] while Ru-Fe nanoparticles supported on carbon nanotubes exhibit enhanced catalytic reactivity compared to monometallic Ru

View Article Online
DOI: 10.1039/D6TA03536A

catalysts.[16] This alloying strategy has been further extended to the design of multicomponent materials. For example, a CoMoFeNiCu high-entropy alloy, identified through optimizing nitrogen adsorption energy, exhibits superior activity for ammonia decomposition.[17] In addition to catalyst discovery, promoter and support engineering also play critical roles. Alkali-promoted Ru catalysts can substantially enhance ammonia decomposition performance under reaction conditions,[18] whereas atomically dispersed Ru atoms on MgO(111)[19] and oxygen-defect-rich CeO_2[20] demonstrate how electronic structures of support and metal-support interactions influence catalytic activity. In parallel, computational studies using electronic structure theories can provide important chemical insights into catalyst design and highly accelerate the discovery process.[21-26] First-principles calculations based on density functional theory (DFT) have identified nitrogen adsorption energy as an effective descriptor for bimetallic catalyst design for ammonia decomposition.[27] Kinetic Monte Carlo simulations on patched Ni-Pt bimetallic surfaces revealed that patches of the Pt metal can create dual Ni active sites that facilitate both ammonia activation and atomic nitrogen association.[28] Additional DFT and microkinetic modeling studies on Ru- and Ir-based catalysts,[29] as well as supported Ru catalysts,[30] consistently showed that NH_x dehydrogenation is kinetically accessible, whereas N_2 formation and desorption remain the rate-limiting step.[31] Despite these elegant advances, given the high scarcity of Ru, arguably the most attractive catalytic metal for NH_3 decomposition, modeling of alloy compositions that aim to maximize the atom efficiency and reactivity of Ru warrants greater attention.

Recently, single-atom alloys (SAAs), in which isolated active metal atoms are atomically dispersed within a host metal matrix, have gained increasing attention in various catalytic reactions.[32-34] Owing to their isolated active sites and tunable dopant-host interfacial environments, SAAs can decouple adsorption and transition state sites, enabling simultaneous weakening of adsorption energies and facile reaction kinetics. This unique capability allows for targeted mitigation of activity and selectivity bottlenecks while maximizing the atomic efficiency of active metal centers. A DFT study of 12 SAAs (Ni-, Pd-, Pt-, and Rh-doped Cu(111), Ag(111), and Au(111)) confirmed the ability of SAAs in weakening intermediate binding strength and reducing activation barriers for several bond activation reactions, including NH_3 activation.[35] Another DFT study showed that dilute metal alloys, including SAAs, are capable of modifying the scaling relations and identified Nb-doped Ag(111) as an active SAA for ammonia synthesis, further highlighting their potential in nitrogen chemistry.[36] Though the development of SAA catalysts for

View Article Online
DOI: 10.1039/D6TA03536A

ammonia decomposition remains limited, a recent DFT study reported that atomically dispersing Ru on a Cu nanocluster can retain favorable ammonia activation while altering intermediate binding relative to their pure metals.[37]

Despite these proof-of-concept studies, a systematic investigation of designing SAAs for ammonia decomposition, along with a fundamental understanding of the underlying chemistry, remains lacking. In this work, we employed first-principles DFT calculations to systematically investigate 23 Ru-doped SAAs spanning selected 3*d*-5*d* host metals for ammonia decomposition toward on-demand hydrogen production. Here, Ru is chosen as the active dopant because of its strong intrinsic capability for N-H bond cleavage,[12, 13] whereas the host metals are expected to modulate the binding strength of nitrogen-containing intermediates and facilitate the associative desorption of adsorbed nitrogen and hydrogen. We first evaluated the thermodynamic stability of these Ru-doped SAAs to assess their resistance against dopant aggregation and subsurface segregation. On identified stable SAAs, we then examined the reaction energies and activation barriers of ammonia dehydrogenation and associative desorption of N_2 and H_2. This study provides mechanistic insights into how host metals regulate catalytic behaviors of Ru-doped SAAs and establishes design principles for developing efficient catalysts for hydrogen production from ammonia decomposition.

II. Computational Methods

Spin-polarized DFT calculations were performed using the Vienna *Ab initio* Simulation Package (VASP).[38, 39] The electrons were described by an all-electron, frozen-core, projector augmented-wave (PAW) method.[40] The electron exchange and correlation were approximated using the Perdew-Burke-Ernzerhof (PBE) functional.[41] Dispersion correction was included using Grimme's D3 method with Becke-Johnson damping.[42, 43] We used a plane-wave kinetic energy cutoff of 500 eV and Monkhorst-Pack *k*-point meshes of 15×15×15 for bulk and 5×5×1 for slab models. All structures were optimized until the electronic energy and ionic force convergence criteria reach 1.0×10^{-6} eV and 0.03 eV/Å, respectively. To construct the Ru-doped SAA surfaces, we used 4×4×1 supercells of the host metals. Details of the rationale for selecting host metals and their facets are provided in SI Figure S1, with representative slab configurations shown in SI Figure S2. We used the most stable crystal structures and facets of each host metal, including hexagonal close-packed or hcp(0001), body-centered cubic or bcc(110), and face-centered cubic or fcc(111), to provide a

View Article Online
DOI: 10.1039/D6TA03536A

consistent basis for comparison across the different hosts. Therefore, the trends reported in this work should be interpreted primarily as composition-dependent catalytic trends rather than as quantitative predictions of the behavior of realistic Ru-doped SAA nanoparticles with complex morphologies. Facet-dependent reactivity of the most promising Ru-doped SAAs identified in this work is the subject of ongoing work. Each SAA slab model was generated by substituting a host atom with a Ru atom in the topmost layer. All SAA slab models consist of four layers, with atoms in the topmost two layers relaxed and atoms in the bottommost two layers fixed at their bulk atomic positions. We added a vacuum region of at least 15 Å along the normal direction to the surface to avoid interactions between the periodic images. We used VASPKIT[44] to construct slab structures, including fixing layers and adjusting ordering of atoms. We note that all calculations in this work were performed using single adsorbates per slab model and therefore represent the low coverage limit. Under realistic reaction conditions, especially at high ammonia pressures, multiple ammonia decomposition intermediates may coexist on the surface. Lateral adsorbate interactions and coverage-dependent effects can alter reaction energies and reaction barriers. Consequently, the trends reported here should be interpreted as reactivity trends under low coverage condition.

Thermodynamic stability, i.e., whether the dopant-host pair can form a SAA structure, of Ru-doped SAAs was evaluated using aggregation (ΔE_{agg}) and segregation (ΔE_{seg}) energies.[26] The aggregation energy quantifies the thermodynamic driving force of Ru atoms to form a surface cluster instead of an isolated surface dopant and was defined as:

$$\Delta E_{agg} = E_{cluster} + (n-1)E_{host} - nE_{SAA}$$

where $E_{cluster}$, E_{host}, and E_{SAA} denote the total energies of a slab containing an n-atom Ru cluster, a slab consisting of host metals only, and a Ru-doped SAA slab, respectively. In this work, a dopant Ru dimer embedded on the host metal surface was adopted to represent the formation of a dopant cluster, corresponding to $n = 2$. Segregation energy was employed to assess the thermodynamic preference of Ru staying in the surface layer of the host relative to migrating into the bulk host metals and was calculated as:

$$\Delta E_{seg} = E_{sub} - E_{SAA}$$

where E_{sub} is the energy of the host metal slab containing a subsurface Ru atom. Within the above definitions, positive values for both ΔE_{agg} and ΔE_{seg} indicate the formation of Ru-doped SAAs against Ru aggregation and segregation. The adsorption energy (E_{ads}) of reaction intermediates was calculated as:

View Article Online
DOI: 10.1039/D6TA03536A

$$E_{ads} = E_{slab+ads} - E_{slab} - E_{adsorbate}$$

where $E_{slab+ads}$, E_{slab}, and $E_{adsorbate}$ represent the total energies of the adsorbate-bound slab, the clean slab, and the isolated adsorbate, respectively. Minimum energy pathways (MEPs) for ammonia decomposition were optimized using the climbing-image nudged elastic band (CI-NEB) method,[45] with initial pathway structures generated by image-dependent pair potential (IDPP) interpolation.[46] Depending on the complexity of each step, five to seven intermediate images were used between the initial and final states. The MEPs were converged until the maximum residual force on each image was below 0.05 eV/Å. To consider temperature effects, we calculated reaction free energies and activation free energies for ammonia decomposition on pure Ru and Ru/Fe SAA at a representative reaction condition of 400 °C (773.15 K) by including zero-point energy, thermal, and entropic contributions (SI Tables S6, S7, and Figure S12). Adsorbed intermediates and transition states were treated within the harmonic approximation, whereas gas-phase molecules were described using ideal gas thermochemistry.

III. Results and Discussion

A. Evaluating the stability of Ru-doped SAAs.

In this work, we considered 23 host elements spanning 3*d*, 4*d*, and 5*d* transition metals, using their most stable bulk crystal structures and facets (SI Figures S1, S2). Several host metals were excluded because their physicochemical properties make them impractical as catalysts. Specifically, Mn was excluded because of its strong oxophilicity and tendency toward surface oxidation under catalytic conditions. Tc was excluded due to its radioactivity. La was not included owing to its complex crystal structure and associated DFT convergence problems. Re and Os were excluded because of their strong affinity for nitrogen-containing adsorbates, which is expected to make them unfavorable for ammonia decomposition. Hg was not considered since it is in liquid phase under ambient conditions and is toxic. After exclusions of the above host metals, 23 Ru-doped SAAs were created for subsequent DFT studies.

Before evaluating their catalytic reactivity, we first assessed whether the 23 Ru-host combinations can form SAAs through evaluating the aggregation and segregation energies, as defined in the Computational Methods section. These two quantities define the two primary thermodynamic instabilities of forming an isolated Ru dopant in SAAs, namely aggregation into forming Ru clusters and migration from surface layer into bulk host metals, as commonly

View Article Online
DOI: 10.1039/D6TA03536A

considered of SAA stability in previous studies.[47-49] Under our definition of aggregation and segregation energies, positive values for both quantities indicate formation of Ru-doped SAAs. For practical SAA synthesis, however, such a 0 K condition can be restrictive and temperature entropic effects may contribute an energy of -0.25 eV to both quantities, and thus we assumed such entropic contributions on top of our DFT-predicted aggregation and segregation energies, consistent with our prior studies.[26] We note that this -0.25 eV entropic contribution was introduced only for evaluating thermodynamic stability and was not applied to reaction energetics. Temperature effects on catalytic reactivity were instead evaluated through explicit free energy calculations for the most promising SAA catalyst (*vide infra*). Based on the above criterion, we classified the 23 Ru-host combinations into three groups (Figure 1, SI Table S1). The first group comprises 10 SAAs, including Ru/Ti (the notation A/B denotes a single atom A atomically dispersed in the surface layer of host B), Ru/V, Ru/Cr, Ru/Fe, Ru/Co, Ru/Ni, Ru/Nb, Ru/Mo, Ru/Ta, and Ru/W SAAs, all of which have positive aggregation and segregation energies assuming a 0.25 eV entropic contribution. We included these 10 stable SAAs in our subsequent catalytic studies. Ru-host combinations in the second group, consisting of Ru/Sc, Ru/Y, Ru/Zr, and Ru/Hf, are not stable due to their unfavorable aggregation energies, indicating formation of Ru clusters. Ru-host combinations in the third group, including Ru/Cu, Ru/Zn, Ru/Rh, Ru/Pd, Ru/Ag, Ru/Cd, Ru/Ir, Ru/Pt, and Ru/Au, are also unstable, but mainly due to their negative segregation energies, indicating diffusion of Ru atoms into host bulk. Ru-host combinations in the second and third groups are not considered in the reactivity studies since they cannot form SAAs.

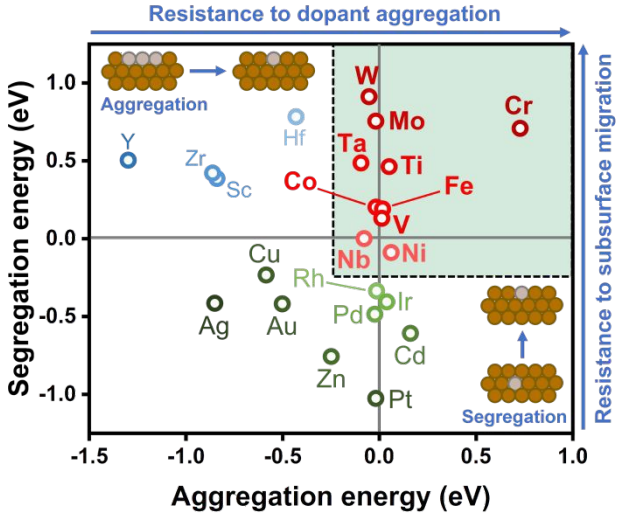

View Article Online
DOI: 10.1039/D6TA03536A

Figure 1. Segregation energy plotted against aggregation energy for 23 Ru-doped SAAs. The green shaded region represents the formation of SAAs, where both aggregation and segregation energies are positive assuming a 0.25 eV entropic contribution. Red symbols indicate formation of SAAs, while blue and green symbols represent dopant clustering and subsurface segregation, respectively. SAAs are labeled in terms of the host metal element. Schematic of dopant aggregation and segregation is shown in the inset.

Our DFT-predicted stability of SAAs using aggregation and segregation energies is supported by several recent experimental studies reporting the synthesis of Ru-based SAAs. For example, Ru/Ni SAA has been synthesized, with isolated Ru atoms characterized by aberration-correction high-angle annular dark-field scanning transmission electron microscopy (AC-HAADF-STEM), *in situ* diffuse reflectance infrared Fourier transform spectroscopy (DRIFTS), and extended X-ray absorption fine structure (EXAFS), for selective hydrogenation of nitroarenes.[50] Likewise, Ru/Co SAAs have been reported in several experimental studies for applications ranging from Fischer-Tropsch synthesis to electrocatalytic reduction of nitrate to ammonia.[51, 52] Ru/Fe SAA has also been experimentally synthesized, with EXAFS confirming the presence of isolated Ru atoms within the Fe host.[53] Together, these experimental studies support the robustness of our DFT framework for evaluating SAA stability while also revealing that only a small fraction of possible SAAs have been realized experimentally.

B. Thermodynamic favorability of ammonia decomposition on stable Ru-doped SAAs.

We first examined the adsorption behavior of intermediates involved in ammonia decomposition on the 10 stable Ru-doped SAAs identified above. Since the selected host metals adopt hcp, bcc, and fcc lattices, we considered all possible adsorption sites, including atop, bridge, hcp hollow, and fcc hollow sites. For bcc(110) surfaces, we further considered two distinct bridge sites, short- and long-bridge sites (SI Figure S3). We highlight that we only considered adsorption sites around the Ru dopant, i.e., Ru site or Ru-host interfacial sites, consistent with the established understanding that the dopants serve as the primary active sites, while the surrounding host atoms modulate the local electronic structures and, consequently, the binding strength.[54, 55] We optimized the adsorption configurations of $*NH_2$, *NH, *N, *H, $*N_2$, and $*H_2$ at the adsorption sites described above on the 10 stable Ru-doped SAAs (SI Figure S4 and Table S2). Specifically, $*NH_2$ and *NH preferentially adsorb at bridge or hollow sites, and *N is more stabilized at bridge sites, particularly the long-bridge sites on SAAs with bcc(110) surfaces. In contrast, $*N_2$ and $*H_2$

View Article Online
DOI: 10.1039/D6TA03536A

typically adsorb at atop sites. For Ru/V SAA, H_2 spontaneously desorbs upon formation. The predicted adsorption energies reveal that tuning the host metal in SAAs can effectively change the binding strength of ammonia decomposition intermediates (SI Table S3). Early transition-metal hosts, such as Ti, V, Nb, and Ta, strengthen the adsorption of nitrogen-containing intermediates, particularly *N and *N_2, whereas late transition-metal hosts, such as Co and Ni, lead to weaker binding. This trend reflects the intrinsic thermodynamic trade-off in ammonia decomposition, where stronger binding might facilitate NH_x dehydrogenation but impede the removal of nitrogen-containing species. This finding is in line with prior studies showing that catalyst performance is governed by the energetic balance among competing elementary steps.[11, 56] Within the Ru-doped SAAs studied here, this balance is modulated by the local Ru-host environment.

We next evaluated the thermodynamic favorability, i.e., reaction energies, of ammonia decomposition on the 10 Ru-doped SAAs (Figure 2 and SI Table S4). Across all systems studied here, NH_x dehydrogenation remains thermodynamically accessible, with negative or slightly positive reaction energies. The first two N-H bond cleavage steps are exothermic on all SAAs, with NH_3 dehydrogenation to *NH_2 and *H ranging from -1.21 eV on Ru/Ni SAA to -2.43 eV on Ru/Ta SAA, and subsequent dehydrogenation of *NH_2 to *NH and *H ranging from -0.32 eV on Ru/Ni SAA to -1.32 eV on Ru/Ta SAA. The final dehydrogenation step from *NH to *N and *H is generally exothermic, although it remains slightly endothermic on Ru/Cr, Ru/Ni, and Ru/W SAAs with reaction energies less than 0.15 eV. These results indicate that the isolated Ru site largely preserves its intrinsic ability to activate ammonia, while host metal atoms modulate the stabilization of dehydrogenated intermediates. Specifically, Ti, V, Nb, and Ta host metals make NH_x dehydrogenation more exothermic, consistent with their stronger binding strength of nitrogen-containing species. The energetics of N_2 formation and desorption exhibits a stronger dependence on host metals. The recombination of *N to form *N_2 is endothermic on most SAAs and is particularly unfavorable on Ru/Ti, Ru/V, and Ru/Ta SAAs, with reaction energies of 2.76, 1.98, and 1.99 eV, respectively. By comparison, this step is much more favorable on Ru/Co SAA with a reaction energy of 0.41 eV and even becomes slightly exothermic on Ru/Ni SAA (-0.12 eV). A similar trend is found for N_2 desorption, which requires large energies on Ru/Ti, Ru/V, Ru/Nb, and Ru/Ta SAAs, with desorption energies of 2.82, 2.15, 2.10, and 2.29 eV, respectively, but is substantially lower on Ru/Fe, Ru/Co, and Ru/Ni SAAs, with values of 0.95, 0.96, and 0.93 eV, respectively. The associative desorption of *H is less sensitive to the host, with *H_2 formation

View Article Online
DOI: 10.1039/D6TA03536A

energies ranging from 0.56 to 1.74 eV, and relatively facile *H_2 desorption energies on several SAAs, including Ru/Ti, Ru/Fe, and Ru/Nb, with values of 0.05, 0.09, and 0.06 eV, respectively. Ru/V is not shown in Figure 2(c) because no stable *H_2 intermediate exists on this surface. Overall, these thermodynamic analyses show that associative desorption of N_2 and H_2, rather than ammonia activation, constitutes the dominant thermodynamic bottleneck across the Ru-doped SAAs.

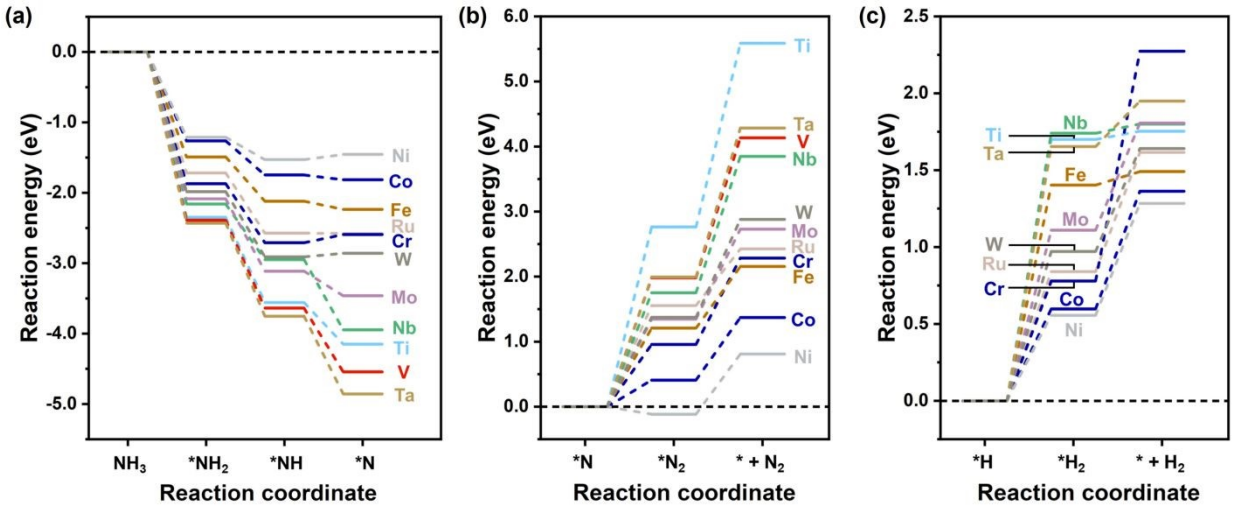

Figure 2. Energy landscapes of (a) stepwise dehydrogenation of NH_3, (b) associative desorption of N_2, and (c) associative desorption of H_2. Ru/V is omitted from panel (c) because *H_2 spontaneously desorbs upon formation. SAAs are labeled in terms of the host metal element.

To rationalize these trends and identify the optimal SAA catalysts for ammonia decomposition, we constructed a thermodynamic map correlating the largest dehydrogenation energy among the three N-H bond-breaking steps with the largest associative desorption energy between N_2 and H_2 formation (Figure 3). This analysis provides an overall picture of the thermodynamic bottlenecks governing ammonia decomposition. The horizontal axis corresponds to the most energy-demanding dehydrogenation step and therefore reflects the accessibility of ammonia activation, whereas the vertical axis represents the most unfavorable associative desorption step and thus captures the thermodynamic limitation associated with product release. In general, all SAAs exhibit the largest dehydrogenation energies below 0.2 eV, indicating that NH_x activation remains thermodynamically accessible. However, associative desorption energies are generally positive as the potential rate-limiting steps and show strong host metal-dependent variation. Systems such as Ru/Ti, Ru/V, Ru/Nb, and Ru/Ta SAAs exhibit highly positive associative desorption energies for both N_2 and H_2, consistent with their strong adsorption of reaction intermediates. The pure Ru surface, used here as a benchmark reference, exhibits a largest

View Article Online
DOI: 10.1039/D6TA03536A

associative desorption energy of 2.42 eV. Among the stable SAAs, Ru/Cr, Ru/Fe, Ru/Co, and Ru/Ni SAAs all show lower associative desorption energies than pure Ru. Ru/Cr provides only a modest improvement, reducing this value to 2.29 eV, whereas Ru/Fe decreases it to 2.15 eV, and Ru/Co and Ru/Ni exhibit much larger reductions to 1.37 and 1.28 eV, respectively. These results highlight the unique capability of Ru-doped SAAs to lower reaction energies relative to pure Ru while maximizing the atomic efficiency of precious Ru. Consequently, Ru/Fe, Ru/Co, and Ru/Ni SAAs combine substantially reduced associative desorption energies with thermodynamically accessible dehydrogenation, and therefore were identified as the most thermodynamically favorable SAA catalysts for ammonia decomposition for subsequent kinetic studies. Importantly, all three top-performing candidates have already been experimentally synthesized,[50-53] highlighting the practical relevance of these predicted catalysts.

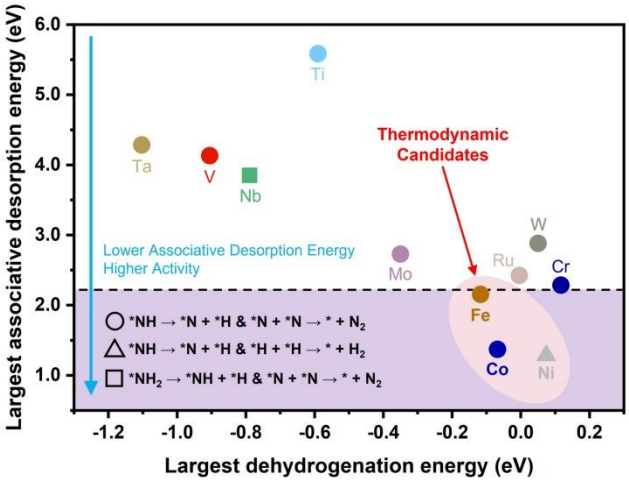

Figure 3. The largest dehydrogenation energy plotted against the largest associative desorption energy between N_2 and H_2 formation. The purple shaded region highlights promising candidates with lowest associative desorption energies, i.e., Ru/Fe, Ru/Co, and Ru/Ni SAAs. Different symbols represent different steps with the largest reaction energies, as shown in the inset.

C. Kinetic study of ammonia decomposition on pure Ru, Ru/Fe, Ru/Co, and Ru/Ni SAAs.

To further assess whether the thermodynamically favorable SAA candidates are also kinetically viable, we evaluated the reaction barriers for ammonia decomposition on the identified Ru/Fe, Ru/Co, and Ru/Ni SAAs, using pure Ru as a benchmark reference (Figure 4, SI Figures S5-S8). For all systems, we considered sequential N-H bond cleavage from $*NH_3$ to *N, followed by associative N-N and H-H combination to form N_2 and H_2. These pathways are consistent with the generally accepted mechanisms of ammonia decomposition on Ru-based catalysts for hydrogen

View Article Online
DOI: 10.1039/D6TA03536A

production, in which NH_x dehydrogenation is kinetically accessible, whereas the removal of surface nitrogen species is often rate-limiting.[29, 57] In addition, this pathway represents the most widely studied mechanism for ammonia decomposition in previous DFT calculations, especially under the elevated temperature and low coverage conditions considered in this work. This mechanism also provides a consistent basis for comparing Ru-doped SAAs. However, alternative pathways involving partially hydrogenated N_2H_x species have been proposed under lower temperature or higher pressure conditions.[58]

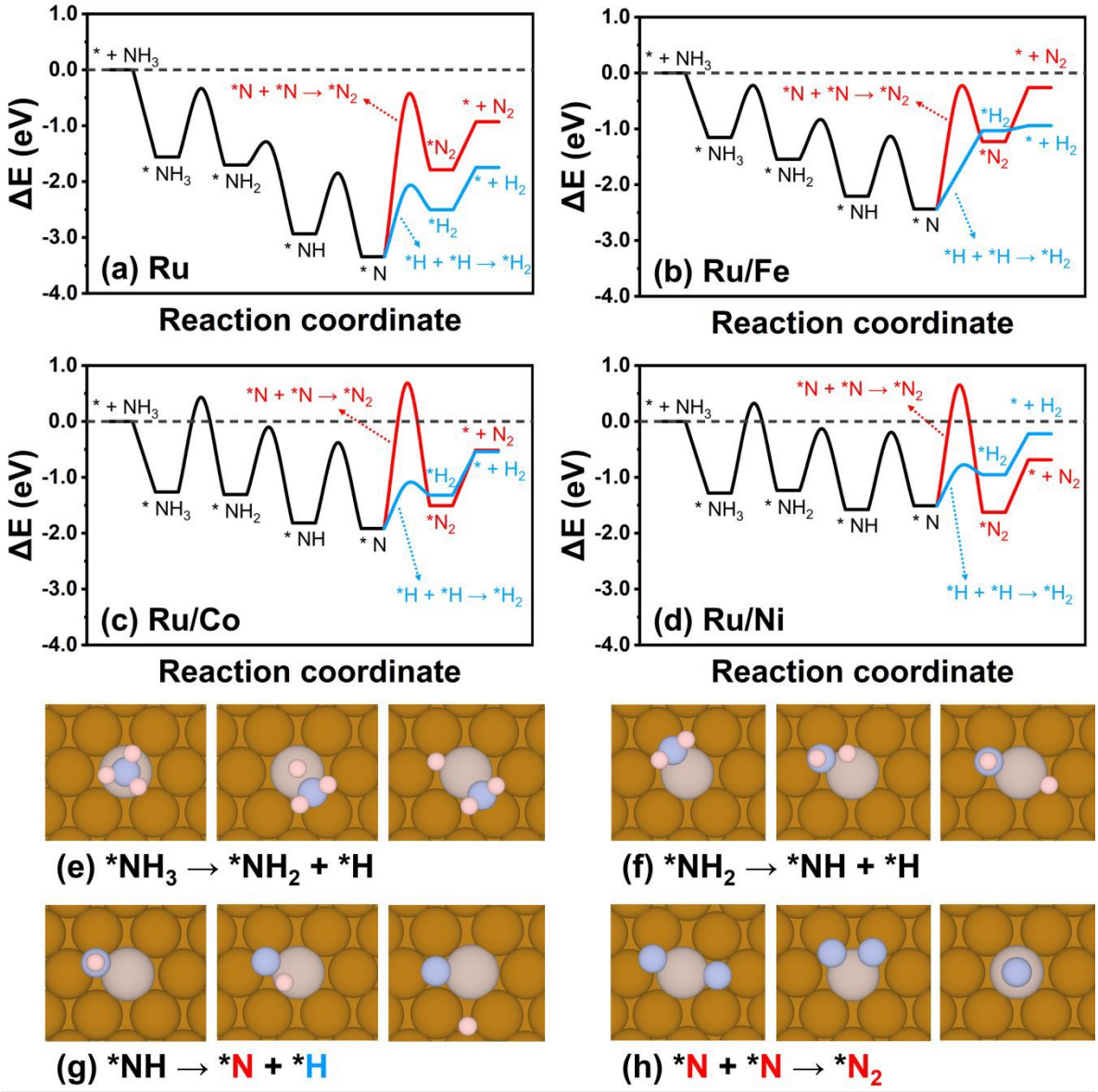

Figure 4. Energy landscapes for ammonia decomposition on (a) pure Ru, (b) Ru/Fe, (c) Ru/Co, and (d) Ru/Ni SAAs. Black lines indicate dehydrogenation steps of NH_3 to adsorbed *N. Red lines

View Article Online
DOI: 10.1039/D6TA03536A

represent associative desorption of N_2 from two *N intermediates, while blue lines indicate associative desorption of H_2 from two *H intermediates. Critical structures (initial, transition, and final states) for (e) $*NH_3 \rightarrow *NH_2 + *H$, (f) $*NH_2 \rightarrow *NH + *H$, (g) $*NH \rightarrow *N + *H$, and (h) $*N + *N \rightarrow *N_2$ on Ru/Fe SAA, respectively. Atoms are colored as follows: Ru in light gray, Fe in brown, N in blue, and H in light pink. For Ru/Fe SAA, no transition state was identified for the H_2 formation.

For pure Ru(0001), widely recognized as the most active monometallic catalyst for ammonia decomposition, the activation barriers for $*NH_3 \rightarrow *NH_2 + *H$, $*NH_2 \rightarrow *NH + *H$, and $*NH \rightarrow *N + *H$ are 1.23, 0.36, and 1.08 eV, respectively, indicating that ammonia activation and subsequent N-H bond cleavage proceed with moderate barriers (Figure 4a). In contrast, the associative N-N combination step ($*N + *N \rightarrow *N_2$) exhibits a much higher barrier of 2.88 eV, which is the largest along the overall reaction pathway and therefore is identified as the rate-limiting step on pure Ru. This result is consistent with prior theoretical and microkinetic studies showing that the strong stabilization of atomic nitrogen on Ru surfaces leads to a substantial kinetic barrier for N_2 formation and desorption.[29, 56, 59] The H-H combination step ($*H + *H \rightarrow H_2$) on pure Ru has a barrier of 1.25 eV, indicating that hydrogen removal is kinetically less demanding than nitrogen removal. Overall, while pure Ru exhibits surmountable dehydrogenation barriers, its activity remains limited by the sluggish removal of adsorbed nitrogen.

For Ru/Fe SAA, the isolated Ru site largely preserves the intrinsic reactivity of pure Ru for ammonia dehydrogenation, consistent with previous studies showing that Ru-centered sites catalyze ammonia activation, whereas the surrounding environment mainly modulates subsequent reaction steps.[19, 37] Surprisingly, isolation of Ru within the Fe host even lowers the barriers for the first and third dehydrogenation steps to 0.93 and 1.07 eV, respectively, compared with 1.23 and 1.08 eV on pure Ru (Figure 4b). More importantly, the barrier for $*N_2$ formation decreases substantially from 2.88 eV on pure Ru to 2.18 eV, showing that the surrounding Fe atoms effectively modulate the electronic structures of the active sites and thereby reduce kinetic limitations. This trend is fully consistent with the thermodynamic analysis above, showing that Ru/Fe SAA weakens the binding of nitrogen-containing intermediates while retaining favorable dehydrogenation energetics. H_2 formation is predicted to be barrierless, with both the reaction energy and barrier being 1.40 eV. Overall, Ru/Fe SAA exhibits similar or even lower barriers for dehydrogenation steps, together with a substantially reduced barrier for N_2 associative desorption

View Article Online
DOI: 10.1039/D6TA03536A

indicating enhanced reactivity for ammonia decomposition while using only a small fraction of precious Ru.

For Ru/Co SAA, the kinetic performance is not improved as systematically as for Ru/Fe. The first N-H bond cleavage becomes less favorable, with a barrier of 1.69 eV, indicating that ammonia activation becomes kinetically more difficult than on pure Ru (Figure 4c). Although the barrier for $*N_2$ formation is slightly reduced relative to pure Ru, it remains high at 2.60 eV, suggesting that *N removal is still challenging on this surface. However, Ru/Co exhibits improved kinetics for *H removal, with an $*H_2$ formation barrier of 0.81 eV. These results indicate that the Co environment facilitates H_2 formation but does not promote N_2 formation to the same extent as Fe. Thus, compared with pure Ru, Ru/Co provides only modest kinetic improvement for the rate-limiting N_2 associative desorption step, but at the expense of the first dehydrogenation step.

Ru/Ni SAA behaves differently from Ru/Fe and Ru/Co. Although the first dehydrogenation step becomes less favorable, with a barrier of 1.61 eV, the barrier of $*N_2$ formation decreases remarkably to 2.16 eV, representing the lowest value for the rate-limiting step among the three SAAs and pure Ru (Figure 4d). This result indicates that Ru-Ni synergy is particularly effective in facilitating associative nitrogen desorption. In addition, Ru/Ni exhibits the lowest $*H_2$ formation barrier, with a value of 0.71 eV. Thus, Ru/Ni performs particularly well for both associative desorption steps, although it is less kinetically favorable for dehydrogenation than Ru/Fe.

Overall, an optimal catalyst is not achieved by minimizing the barrier of a single elementary step, but rather by balancing performance across the entire reaction pathway. Although Ru/Ni exhibits the lowest barrier for N_2 formation (2.16 eV), its dehydrogenation steps are less favorable than those on Ru/Fe. Ru/Co shows improved kinetics for H_2 formation, but it still suffers from a high barrier for N_2 formation. In contrast, Ru/Fe combines low barriers for ammonia dehydrogenation with a substantially reduced barrier for N_2 formation (2.18 eV), compared to the 2.88 eV of pure Ru. Based on the reaction energies and reaction barriers of both dehydrogenation and associative desorption, Ru/Fe exhibits the most favorable catalytic characteristics among the SAAs considered in this work, and is therefore identified as the most promising SAA catalyst for hydrogen production through ammonia decomposition. Further consideration of temperature effects through free energy calculations shows that the inclusion of temperature corrections shifts the reaction barriers by similar amounts between pure Ru and Ru/Fe SAA across all steps (SI Figure S12 and Table S7). In addition, the activation free energy of the rate-limiting N_2 formation

View Article Online
DOI: 10.1039/D6TA03536A

step on Ru/Fe SAA remains 2.18 eV, still substantially lower than the corresponding barrier of 2.87 eV on pure Ru (SI Figure S12 and Table S7), confirming that Ru/Fe remains the most promising catalyst for ammonia decomposition. To further evaluate the kinetic significance of the reduced N_2 formation barrier on Ru/Fe, we estimated rate constants using transition state theory (SI Table S7). Based on the predicted free energy barriers at 773.15 K, the rate constant for *N + *N → *N_2 increases from 3.2×10^{-6} s^{-1} on pure Ru to 9.9×10^{-2} s^{-1} on Ru/Fe SAA, leading to an approximately 3.1×10^{4}-fold enhancement. Although these values represent elementary step rate constants rather than realistic turnover frequencies, the results demonstrate that the reduced N_2 formation barrier on Ru/Fe translates into a substantial kinetic advantage over pure Ru. In this study, pure Ru was used as the benchmark system for evaluating the effects of Ru doping into different host metals. We acknowledge that numerous Ru-based catalysts, including promoted, supported, and alloyed Ru systems, have been reported to exhibit enhanced activity for ammonia decomposition relative to pure Ru. Previous studies generally report reductions in activation barrier by approximately 0.2 - 0.6 eV compared with their corresponding Ru-based references.[18, 19, 60] The barrier reduction predicted for Ru/Fe SAA is comparable to or greater than many of these reported values, suggesting that Ru/Fe SAA is a promising Ru-based catalyst for ammonia decomposition. More importantly, Ru/Fe SAA has recently been synthesized and experimentally characterized,[53] demonstrating that the most promising catalyst identified in this study is experimentally accessible and can serve as a platform for further catalyst development and performance optimization.

D. Developing reactivity descriptor for ammonia decomposition on Ru-doped SAAs.

Given the large chemical space of SAAs arising from variations in dopants, host metals, and surface facets, we next sought to develop a physically interpretable descriptor capable of rationalizing activity trends across these systems. Because catalytic performance is governed by both NH_x dehydrogenation and *N associative desorption, an effective descriptor should capture both the binding strength and activation of nitrogen species. We first examined the scaling relationships among the adsorption energies of N-containing intermediates (SI Figure S9). When referenced against the *N adsorption energy, we observed strong linear correlations for *N_2 and *NH, with coefficients of determination (R^2) of 0.87 and 0.81, respectively, whereas the correlation for *NH_2 is relatively weaker, with an R^2 of 0.57. When *N_2 is used as the reference,

View Article Online
DOI: 10.1039/D6TA03536A

the correlations for *NH and *NH_2 decrease, with R^2 values of 0.68 and 0.64. These results indicate that the adsorption energies of nitrogen species on Ru-doped SAAs remain partially coupled, consistent with the descriptor-based framework commonly used in heterogeneous catalysis.[61] However, some of the moderate R^2 values suggest that linear scaling relations are not fully preserved in the SAA systems. Such deviations are expected for SAAs, whose distinct electronic structures can weaken or disrupt the adsorption trends commonly observed on monometallic surfaces.[62]

To elucidate the correlation between reaction energies and activation barriers, we next examined whether Brønsted-Evans-Polanyi (BEP) relationships hold for the NH_x dehydrogenation steps (SI Figure S10). In general, linear correlations are observed between activation barriers and reaction energies for the three N-H bond cleavage steps. The overall R^2 value is 0.74 across pure Ru and the three SAAs (Ru/Fe, Ru/Co, and Ru/Ni), while stronger correlations are obtained for individual surfaces, with R^2 values of 0.90 for Ru, 0.99 for Ru/Fe, 0.82 for Ru/Co, and 0.80 for Ru/Ni. The corresponding slopes range from 0.73 to 1.08, indicating that the sensitivity of activation barriers to reaction energies varies across different systems. These results confirm that the kinetics of NH_x dehydrogenation are correlated with thermodynamic favorability.[56] More importantly, since reaction energies are fundamentally governed by the binding strengths of reactant and product species, the BEP relationships establish a direct connection between adsorption energies and reaction barriers, suggesting that adsorption energies may serve as effective descriptors for the reactivity of SAAs for ammonia decomposition.

Motivated by the BEP relationships established above, we then evaluated whether the adsorption energy of *N could serve as a descriptor for the overall reactivity of SAAs in ammonia decomposition (Figure 5). Gratifyingly, the adsorption energy of *N shows strong correlations with both the largest reaction energy among the three dehydrogenation steps and that among the two associative desorption steps, with R^2 values of 0.73 and 0.95, respectively, across all SAAs, despite different systems might exhibit different rate-determining steps. Importantly, dehydrogenation energetics display a positive correlation with *N adsorption energy, while associative desorption energetics exhibit a negative correlation, reflecting the intrinsic trade-off between these two classes of reactions governed by *N binding strength. Since the associative desorption of N_2 is rate-limiting, identifying systems with relatively weaker *N binding, such as Ru/Fe, Ru/Co, and Ru/Ni, is critical for improving catalytic performance. These results indicate

View Article Online
DOI: 10.1039/D6TA03536A

that *N adsorption energy is an effective descriptor for identifying promising SAA catalysts. We note that the *N adsorption energy exhibits a systematic correlation with reaction energies across pure Ru and all stable Ru-based SAAs considered in this work and therefore serves primarily as a thermodynamic descriptor. The potential correlation between *N adsorption energy and reaction barriers is suggested by the BEP relationship, which was established using only a limited number of surfaces in the present study.

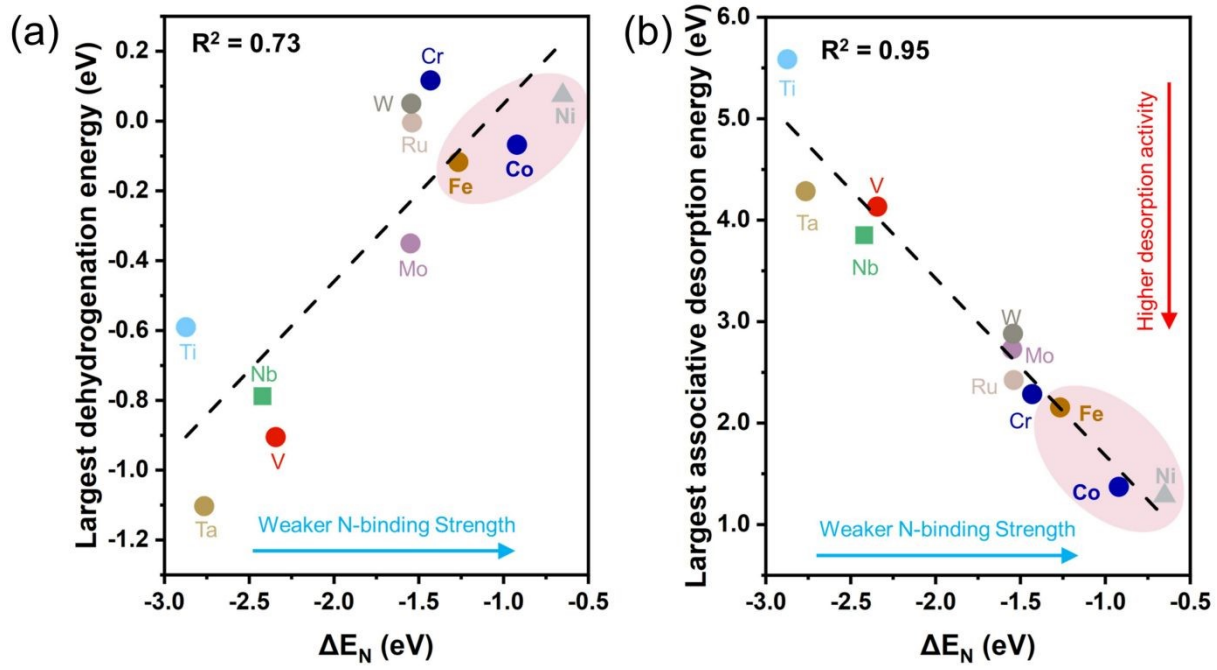

Figure 5. Correlation between *N adsorption energy and (a) the largest dehydrogenation energy, and (b) the largest associative desorption energy. The dashed lines represent the best linear fit with the corresponding R^2 values. The shaded regions highlight promising candidates with lowest associative desorption energies, i.e., Ru/Fe, Ru/Co, and Ru/Ni SAAs. SAAs are labeled in terms of the host metal element. Different symbols represent different steps with the largest reaction energies, consistent with the definition in Figure 3.

To assess whether other descriptors in addition to *N adsorption energy could guide the reactivity, we performed several additional analyses (SI Figure S11). When the adsorption energy of $*N_2$ is used, the correlations are slightly weaker than those obtained with *N adsorption energy, with R^2 values of 0.65 for the largest dehydrogenation energy and 0.92 for the largest associative desorption energy (SI Figures S11a and S11b). Although $*N_2$ adsorption captures the trend, its overall performance remains limited, particularly in the regime of the most promising candidates. We also examined descriptors reported in previous work,[63] which include physicochemical

View Article Online
DOI: 10.1039/D6TA03536A

quantities, such as electronegativity (x), atomic radius (r), coordination number (cn), and adsorption geometry (α) (SI Figures S11c and S11d). Similar approaches have been used to correlate catalyst electronic and geometric parameters with reactivity.[64, 65] While these properties show moderate correlations, with R^2 values of 0.64 and 0.78, they remain less practical since adsorption geometry still requires DFT geometry optimizations and therefore offer little advantage over directly using adsorption energy. Finally, we considered descriptors identified through the sure independence screening and sparsifying operator (SISSO) approach[66] (SI Table S5 and Figures S11e and S11f), which has been applied to identify low-dimensional descriptors in catalytic systems.[67] In our systems, the SISSO-derived descriptors yield R^2 values of 0.78 and 0.80, indicating reasonable predictive capability and potential future applications.

IV. Conclusions

In this work, we employed first-principles DFT calculations to systematically investigate Ru-doped SAAs as catalysts for ammonia decomposition. Starting from a library of 23 SAAs with varying transition-metal hosts, we performed stability screening based on aggregation and segregation energies and identified 10 stable Ru-doped SAAs, namely Ru/Ti, Ru/V, Ru/Cr, Ru/Fe, Ru/Co, Ru/Ni, Ru/Nb, Ru/Mo, Ru/Ta, and Ru/W, in which isolated Ru atoms are thermodynamically resistant to both aggregation into forming a cluster and diffusion into subsurface of host metal. Subsequent thermodynamic analysis showed that NH_x dehydrogenation remains accessible across all stable SAAs, whereas the associative formation and desorption of N_2 exhibit much stronger host dependence and is rate-limiting. Within the 10 stable SAAs, Ru/Fe, Ru/Co, and Ru/Ni are the most promising candidates because they exhibit reduced associative desorption energy while maintaining similar dehydrogenation energy compared to pure Ru.

Kinetic analysis further showed that the catalytic performance is not determined solely by reaction barrier of a single step, but by the overall balance of barriers between ammonia activation and product formation. Pure Ru shows a very high barrier for N_2 formation, consistent with its known tendency toward nitrogen poisoning. Among the three SAA candidates, Ru/Fe exhibits the best overall performance with substantially reduced reaction barriers of N_2 formation and similar barriers for ammonia activation. Ru/Ni shows the lowest N_2 associative desorption barrier, and Ru/Co improves the kinetics of H_2 formation, but at the cost of dehydrogenation barriers. These

View Article Online
DOI: 10.1039/D6TA03536A

results therefore identify Ru/Fe as the most promising Ru-doped SAA candidate for ammonia decomposition.

Finally, we identified the *N adsorption energy as an effective thermodynamic descriptor for ammonia decomposition on Ru-doped SAAs. We observed strong correlations of *N adsorption energy with both the largest dehydrogenation energy and the largest associative desorption energy across all 10 stable SAAs, despite different SAAs having different dehydrogenation or associative desorption steps as the most energy-demanding. Overall, this study provides a fundamental understanding of how dopant-host environments regulate the reactivity of isolated Ru sites, highlights Ru/Fe as a reactive catalyst with highly reduced reliance on precious Ru metals, and develops catalyst design principles for the future screening of SAAs for ammonia decomposition.

Conflicts of interest

There are no conflicts to declare.

Data availability

The data supporting this article have been included as part of the Supplementary Information.

Acknowledgements

The authors acknowledge support by the donors of ACS Petroleum Research Fund under Doctoral New Investigator Grant 68077-DNI5 and by the National Science Foundation under Award No. CBET-2440175 and CBET-2440941. This work used computational resources provided by Research Computing at Northeastern University and Stampede3 at the Texas Advanced Computing Center (TACC) through allocation CHE250137 from the Advanced Cyberinfrastructure Coordination Ecosystem: Services & Support (ACCESS) program.

View Article Online
DOI: 10.1039/D6TA03536A

References

1. S. Chu, Y. Cui and N. Liu, *Nat. Mater.*, 2016, **16**, 16-22.
2. I. Staffell, D. Scamman, A. Velazquez Abad, P. Balcombe, P. E. Dodds, P. Ekins, N. Shah and K. R. Ward, *Energy Environ. Sci.*, 2019, **12**, 463-491.
3. S. J. Davis, N. S. Lewis, M. Shaner, S. Aggarwal, D. Arent, I. L. Azevedo, S. M. Benson, T. Bradley, J. Brouwer, Y. M. Chiang, C. T. M. Clack, A. Cohen, S. Doig, J. Edmonds, P. Fennell, C. B. Field, B. Hannegan, B. M. Hodge, M. I. Hoffert, E. Ingersoll, P. Jaramillo, K. S. Lackner, K. J. Mach, M. Mastrandrea, J. Ogden, P. F. Peterson, D. L. Sanchez, D. Sperling, J. Stagner, J. E. Trancik, C. J. Yang and K. Caldeira, *Science*, 2018, **360**, eaas9793.
4. L. Schlapbach and A. Züttel, *Nature*, 2001, **414**, 353-358.
5. I. A. Hassan, H. S. Ramadan, M. A. Saleh and D. Hissel, *Renew. Sustain. Energy Rev.*, 2021, **149**, 111311.
6. J. Guo and P. Chen, *Chem*, 2017, **3**, 709-712.
7. A. Valera-Medina, H. Xiao, M. Owen-Jones, W. I. F. David and P. J. Bowen, *Prog. Energy Combust. Sci.*, 2018, **69**, 63-102.
8. D. R. MacFarlane, P. V. Cherepanov, J. Choi, B. H. R. Suryanto, R. Y. Hodgetts, J. M. Bakker, F. M. Ferrero Vallana and A. N. Simonov, *Joule*, 2020, **4**, 1186-1205.
9. Z. Zhao, W. He, B. Guo, J. Yu, Z. Wang and H. Yu, *Energy Fuels*, 2025, **39**, 13825-13847.
10. T. Han, L. Wei, S. Xie, Y. Liu, H. Dai and J. Deng, *Ind. Chem. Mater.*, 2025, **3**, 311-331.
11. Y. Song, Y. Ju, C. Son, D. Bae, Y. J. Go, S. B. Kang and M. Kim, *J. Catal.*, 2025, **450**, 116339.
12. Z. Lu, B. Jiang, Z. Chen, J. Shi, D. Jing, Y. Lu and M. Liu, *Innovation Energy*, 2024, **1**, 100056.
13. Z. Su, J. Guan, Y. Liu, D. Shi, Q. Wu, K. Chen, Y. Zhang and H. Li, *Int. J. Hydrogen Energy*, 2024, **51**, 1019-1043.
14. W. Yan, B. Liang, G. Bi, H. Zhuo, W. Wang, H. Duan, G. Xu, F. Wang, Y. Su, T. Zhang, X. Yang and Y. Huang, *ACS Sustain. Chem. Eng.*, 2024, **12**, 15024-15032.
15. S. Chen, J. Jelic, D. Rein, S. Najafishirtari, F. P. Schmidt, F. Girgsdies, L. Kang, A. Wandzilak, A. Rabe, D. E. Doronkin, J. Wang, K. Friedel Ortega, S. DeBeer, J. D. Grunwaldt, R. Schlogl, T. Lunkenbein, F. Studt and M. Behrens, *Nat. Commun.*, 2024, **15**, 871.
16. C. Chen, Y. Chen, A. M. Ali, W. Luo, J. Wen, L. Zhang and H. Zhang, *Chem. Eng. Technol.*, 2020, **43**, 719-730.
17. P. Xie, Y. Yao, Z. Huang, Z. Liu, J. Zhang, T. Li, G. Wang, R. Shahbazian-Yassar, L. Hu and C. Wang, *Nat. Commun.*, 2019, **10**, 4011.
18. S. Sayas, N. Morlanés, S. P. Katikaneni, A. Harale, B. Solami and J. Gascon, *Catal. Sci. Technol.*, 2020, **10**, 5027-5035.
19. H. Fang, S. Wu, T. Ayvali, J. Zheng, J. Fellowes, P. L. Ho, K. C. Leung, A. Large, G. Held, R. Kato, K. Suenaga, Y. I. A. Reyes, H. V. Thang, H. T. Chen and S. C. E. Tsang, *Nat. Commun.*, 2023, **14**, 647.
20. B. Teng, C. Ma, J. Chen, Y. Zhang, B. Wei, M. Sang, H. Wang and Y. Sun, *ACS Appl. Nano Mater.*, 2024, **7**, 15012-15024.
21. C. Zhou, M. Kothakonda and Q. Zhao, *J. Catal.*, 2025, **448**, 116194.
22. C. Zhou and Q. Zhao, *ChemPhysChem*, 2025, **26**, e202401097.

View Article Online
DOI: 10.1039/D6TA03536A

23. C. Gallagher, M. Kothakonda and Q. Zhao, *Phys. Chem. Chem. Phys.*, 2025, **27**, 5464-5475.
24. Q. Zhao, J. M. P. Martirez and E. A. Carter, *Proc. Natl. Acad. Sci. U.S.A.*, 2022, **119**, e2202931119.
25. Q. Zhao, J. M. P. Martirez and E. A. Carter, *J. Am. Chem. Soc.*, 2021, **143**, 6152-6164.
26. M. Kothakonda, S. LaCroix, C. Zhou, J. Yang, J. Su and Q. Zhao, *ACS Catal.*, 2025, **15**, 11608-11616.
27. D. A. Hansgen, D. G. Vlachos and J. G. Chen, *Nat. Chem.*, 2010, **2**, 484-489.
28. W. Guo and D. G. Vlachos, *Nat. Commun.*, 2015, **6**, 8619.
29. X. Lu, J. Zhang, W. K. Chen and A. Roldan, *Nanoscale Adv.*, 2021, **3**, 1624-1632.
30. S. R. Kulkarni, N. Realpe, A. Yerrayya, V. K. Velisoju, S. Sayas, N. Morlanes, J. Cerillo, S. P. Katikaneni, S. N. Paglieri, B. Solami, J. Gascon and P. Castaño, *Catal. Sci. Technol.*, 2023, **13**, 2026-2037.
31. J. Yang, K. Ye, S. Xie, Q. Li, C. Milhans, F. Liu and F. Che, *J. Am. Chem. Soc.*, 2026, **148**, 537-546.
32. G. Giannakakis, M. Flytzani-Stephanopoulos and E. C. H. Sykes, *Acc. Chem. Res.*, 2019, **52**, 237-247.
33. R. T. Hannagan, G. Giannakakis, M. Flytzani-Stephanopoulos and E. C. H. Sykes, *Chem. Rev.*, 2020, **120**, 12044-12088.
34. C. Zhou and Q. Zhao, *Nanoscale*, 2026, **18**, 11007-11024.
35. M. T. Darby, R. Réocreux, E. C. H. Sykes, A. Michaelides and M. Stamatakis, *ACS Catal.*, 2018, **8**, 5038-5050.
36. Y. Zhang, S. Li, C. Sun, P. Wang, Y. Yang, D. Yi, X. Wang and J. Yao, *ACS Catal.*, 2022, **12**, 9201-9212.
37. D. Chattaraj and C. Majumder, *Phys. Chem. Chem. Phys.*, 2023, **26**, 524-532.
38. G. Kresse and J. Furthmüller, *Comput. Mater. Sci.*, 1996, **6**, 15-50.
39. G. Kresse and J. Furthmüller, *Phys. Rev. B*, 1996, **54**, 11169-11186.
40. P. E. Blochl, *Phys. Rev. B*, 1994, **50**, 17953-17979.
41. J. P. Perdew, K. Burke and M. Ernzerhof, *Phys. Rev. Lett.*, 1996, **77**, 3865.
42. S. Grimme, J. Antony, S. Ehrlich and H. Krieg, *J. Chem. Phys.*, 2010, **132**, 154104.
43. S. Grimme, S. Ehrlich and L. Goerigk, *J. Comput. Chem.*, 2011, **32**, 1456-1465.
44. V. Wang, N. Xu, J.-C. Liu, G. Tang and W.-T. Geng, *Comput. Phys. Commun.*, 2021, **267**, 108033.
45. G. Henkelman, B. P. Uberuaga and H. Jónsson, *J. Chem. Phys.*, 2000, **113**, 9901-9904.
46. S. Smidstrup, A. Pedersen, K. Stokbro and H. Jonsson, *J. Chem. Phys.*, 2014, **140**, 214106.
47. T. He, R. Shi, T. Zhou, A. R. Puente Santiago and Q. Liu, *ACS Catal.*, 2025, **15**, 10005-10017.
48. M. Salem and G. Mpourmpakis, *Nanoscale*, 2025, **17**, 2830-2840.
49. M. Salem, D. J. Loevlie and G. Mpourmpakis, *J. Phys. Chem. C*, 2023, **127**, 22790-22798.
50. W. Liu, H. Feng, Y. Yang, Y. Niu, L. Wang, P. Yin, S. Hong, B. Zhang, X. Zhang and M. Wei, *Nat. Commun.*, 2022, **13**, 3188.
51. G. Meng, J. Sun, L. Tao, K. Ji, P. Wang, Y. Wang, X. Sun, T. Cui, S. Du, J. Chen, D. Wang and Y. Li, *ACS Catal.*, 2021, **11**, 1886-1896.
52. X. Zhu, Y. C. Wang, K. Qu, L. Song, J. Wang, Y. Gong, X. Liu, C. F. Li, S. Yuan, Q. Lu and A. L. Wang, *Nat. Commun.*, 2025, **16**, 5742.

View Article Online
DOI: 10.1039/D6TA03536A

53. S. Singh, E. P. Komarala, S.-J. Kim, C. T. Yavuz, L. M. Maghrabi, N. Singh, M. Harfouche, V. Sabastian, O. Malina, A. Bakandritsos, D. H. Anjum, A. A. AlHammadi and K. Polychronopoulou, *Appl. Surf. Sci.*, 2025, **685**, 161906.
54. R. Reocreux, E. C. H. Sykes, A. Michaelides and M. Stamatakis, *J. Phys. Chem. Lett.*, 2022, **13**, 7314-7319.
55. J. Schumann, M. Stamatakis, A. Michaelides and R. Reocreux, *Nat. Chem.*, 2024, **16**, 749-754.
56. A. Logadottir, T. H. Rod, J. K. Nørskov, B. Hammer, S. Dahl and C. J. H. Jacobsen, *J. Catal.*, 2001, **197**, 229-231.
57. X. Duan, J. Zhou, G. Qian, P. Li, X. Zhou and D. Chen, *Chin. J. Catal.*, 2010, **31**, 979-986.
58. X. Zou, H.-Y. Su, X. Sun, W. Pang, X. Hao, Y. Xu and K. Sun, *Appl. Surf. Sci.*, 2024, **649**, 159175.
59. J. J. Mortensen, B. Hammer and J. K. Nørskov, *Phys. Rev. Lett.*, 1998, **80**, 4333-4336.
60. Z. Wang, Z. Cai and Z. Wei, *ACS Sustain. Chem. Eng.*, 2019, **7**, 8226-8235.
61. A. Dasgupta, Y. Gao, S. R. Broderick, E. B. Pitman and K. Rajan, *J. Phys. Chem. C*, 2020, **124**, 14158-14166.
62. M. T. Darby, M. Stamatakis, A. Michaelides and E. C. H. Sykes, *J. Phys. Chem. Lett.*, 2018, **9**, 5636-5646.
63. C. Ren, Y. Cui, Q. Li, C. Ling and J. Wang, *J. Am. Chem. Soc.*, 2025, **147**, 13610-13617.
64. X. Chang, Z. J. Zhao, Z. Lu, S. Chen, R. Luo, S. Zha, L. Li, G. Sun, C. Pei and J. Gong, *Nat. Nanotechnol.*, 2023, **18**, 611-616.
65. H. Xu, J. Wang, J. Liu and D. Cheng, *Acc. Chem. Res.*, 2025, **58**, 2535-2549.
66. R. Ouyang, S. Curtarolo, E. Ahmetcik, M. Scheffler and L. M. Ghiringhelli, *Phys. Rev. Mater.*, 2018, **2**, 083802.
67. Z. K. Han, D. Sarker, R. Ouyang, A. Mazheika, Y. Gao and S. V. Levchenko, *Nat. Commun.*, 2021, **12**, 1833.

View Article Online
DOI: 10.1039/D6TA03536A

The data supporting this article have been included as part of the Supplementary Information.